Research Article

Nonlinear Vibration Characteristics of the Involute Spline Coupling in Aeroengine with the Parallel Misalignment

Xiangzhen Xue [1,2] **Qixin Huo,**[1] **and Jian Liu**[1]

[1]*Shaanxi University of Science & Technology, Xi'an 710021, China*
[2]*Mechanical Innovation and Tribology Group, School of Engineering, University of Birmingham,*
 Edgbaston Birmingham B15 2TT, UK

Correspondence should be addressed to Xiangzhen Xue; a_zheny@163.com

In order to control the vibration of the involute spline coupling in aeroengine well and reduce the fretting wear, a bending–torsion coupling nonlinear vibration model of the involute spline coupling with the misalignment was proposed, and a dynamic meshing stiffness function with multiteeth engagement was established. Then, the influence of different misalignment, wear, and rotation speeds with different misalignment on the nonlinear vibration characteristics of the involute aviation spline coupling was explored. The result shows that with an increase of the parallel misalignment, the system experienced the state of a single period, a quasiperiod, multiperiod, and chaos but finally only alternated between the quasiperiod and the chaos state. The uneven wear of each tooth of the spline displayed a significant influence on the vibration of the spline coupling, and the influence of the uniform wear was smaller under given conditions here. Furthermore, with an increase of the speed, the larger the misalignment was, the more times the system entered or left the chaos state were. The model proposed here is found to be closer to the actual working conditions, and the analysis results can provide more accurate external load conditions for the prediction of the fretting damage of the spline coupling in aeroengine.

1. Introduction

There should be no relative displacement between the involute spline couplings of aeroengine. As the involute spline couplings are not only subjected to a strong external excitation of cycle loads but also the internal excitation introduced by the time-varying meshing stiffness and the error produced in the process of manufacturing or assembly while taking off, cruising, and landing, they exhibit a heavy nonlinear vibration [1–4]. Especially, for the internal and external spline shafts, they are misaligned during installation or misaligned due to heating, loading, and foundation deformation, or there is a misalignment between the involute spline couplings before assembly. Generally, there are three kinds of misalignment in the involute spline coupling: parallel misalignment, angular misalignment, and combined misalignment. The parallel misalignment means two connected rotor axes are

connected with some parallel offset in the radial direction; the angular misalignment means two connected rotor axes are connected with an angle; the combined misalignment means two connected rotor axis lines have both an angle and a parallel offset. All types of misalignment can cause the spline coupling bending, as well as introduce additional loads to the spline shaft. Then, the loads between the teeth is redistributed, which results in a strong bending–torsion coupling nonlinear vibration of the involute spline coupling in aeroengine [5, 6]. On the one hand, due to the bending torsional coupling nonlinear vibration, the smoothness of system transmission will get worse, so there will be much noise [7]; on the other hand, the fretting will be introduced between the two contact surfaces. Further, the fretting wear alters the backlash and the surface roughness of spline teeth, and then affects the vibration excitation of the system and intensifies its vibration characteristics of the system [8–10].

Therefore, there must be some relationship between the fretting wear and the vibration of the spline coupling [11, 12]. Finally, the repeated fretting movement leads to a serious failure of the fretting wear in the spline coupling of aeroengine [13–16]. At present, there are a large number of studies on fretting wear and the vibration characteristics of aviation involute splines, but both of them are two unrelated issues.

In terms of spline coupling vibration, there have been several studies focused on predicting the free and forced vibration characteristics of rotor-coupling systems [17–19]. These studies proposed the vibration model of the system using the finite-element method and analyzed the effect of the spline force on the stability of the rotor system. Theoretical and experimental analyses were conducted the effects of vibration parameters on the vibration characteristics and the stability of the system. However, these studies did not analyze the influence of the misalignment on the vibration characteristics of the system. Though there are numerous studies on the effect of the misalignment on the vibration characteristics of the system, the multiteeth meshing was not in these works [20, 21]. Consequently, the results are not accurate enough for the design of aeroengine involute spline couplings. Only Zhang and Cuffaro take into account the misalignment and investigated the vibration characteristics [22, 23]. Kahraman assumed both the shaft and the gear (or any other component splined to the shaft) deflect only at the spline teeth and investigated the vibration characteristics of involute spline couplings [24].

In terms of the fretting wear of the spline coupling, Leen et al. conducted a study on the characteristic of the friction contact of the helical spline coupling using the finite-element method considering the axial load and torque load and analyzed the influence of the tooth profile modification on the contact stress, sliding distance, and friction factor of the spline teeth [25]. Medina and Olver studied the elastic contact model of the spline coupling based on the boundary finite-element method and explored the influence of large-scale design parameters, torque, and eccentricity error on the contact pressure and the slip distance distribution of the spline coupling [26]. Mccoll proposed a finite-element method to calculate the fretting wear based on the modified Archard's equation and measured the friction coefficient and the wear coefficient by using the friction and wear experiment [27]. In 2003, Ding et al. also proposed a numerical method based on the modified Archard's equation to simulate the fretting wear of a pin disk under the partial sliding and complete sliding, which not only calculated the surface contact pressure and the sliding distance but also calculated the subsurface contact pressure [28]. According to these analyses, the above studies did not investigate the fretting wear on the vibration characteristics of bending–torsion under the internal and external excitation of the system, and Zhao and others only considered the relationship between the fretting wear and the vibration displacement [13, 29, 30].

Therefore, based on the above studies, a bending–torsion coupling nonlinear vibration model of the involute spline coupling with a misalignment was proposed; the working conditions of the parallel misalignment and the displacement on the meshing line in different quadrants of the involute spline coupling were analyzed, and the meshing stiffness of a single tooth under an ideal condition with the parallel misalignment was calculated. Then, the vibration characteristics of the involute spline coupling in the aeroengine system on different parallel misalignment, fretting wear, and speed rotation were studied. It is of great significance for controlling the vibration and reducing the fretting wear failure to study the bending–torsion coupling nonlinear vibration characteristics of the involute splines considering the parallel misalignment.

2. Vibration Model of the System considering the Misalignment

2.1. Establishment of the Vibration Model. The vibration model of the bending–torsion coupling of the involute spline coupling in the aeroengine system in the three-dimensional plane is shown in Figure 1(a). The four concentrated mass blocks marked as 1, 2, 3, and 4 in Figure 1(a) represent the prime mover, external spline, internal spline, and load, respectively. The prime mover with the torsional stiffness k_{T1} and the torsional damping c_{T1} is connected with the external spline using a massless elastic shaft; the internal spline with the torsional stiffness k_{T2} and the torsional damping c_{T2} is connected with the load using a massless elastic shaft; the internal and external splines are connected with the involute teeth, considering the meshing stiffness k_m, meshing damping c_m, and clearance c_i between the working teeth profile and clearance c'_i and between the non-working teeth profile. It is further considered that there are supporting stiffness and supporting damping on the internal and external splines. $k_{px1}, k_{py1}, k_{px2}, k_{py2}$ represent the supporting stiffness of the external spline and the internal spline along the x and the y coordinate axes, respectively; $c_{px1}, c_{py1}, c_{px2}, c_{py2}$ represent the supporting damping of the external spline and the internal spline along the x and the y coordinate axes, respectively; the input torque and the load torque of the system are T_d, T_L, respectively.

The vibration model of the bending–torsion coupling of the involute spline coupling in the aeroengine system in the two-coordinate plane is shown in Figure 1(b). In Figure 1(b), the influence of the misalignment is taken into account.

2.2. Analysis of the Working Conditions of the Misalignment. The misalignment of the involute spline coupling in aeroengine includes parallel misalignment, angular misalignment, and combined misalignment, as shown in Figures 2–4. As the vibration of the involute spline coupling is only analyzed in the xoy plane in this work, the vibration of the z-axis freedom is not considered, and the parallel misalignment in the x and y directions is mainly analyzed. As shown in Figure 3, the black lines represent the external involute spline and its coordinate system, and the red lines represent the internal involute spline and its coordinate system. Here, it is assumed that the external spline is stationary under the parallel misalignment condition. Therefore, the misalignment is introduced from the movement of the internal spline. From

(a)   (b)
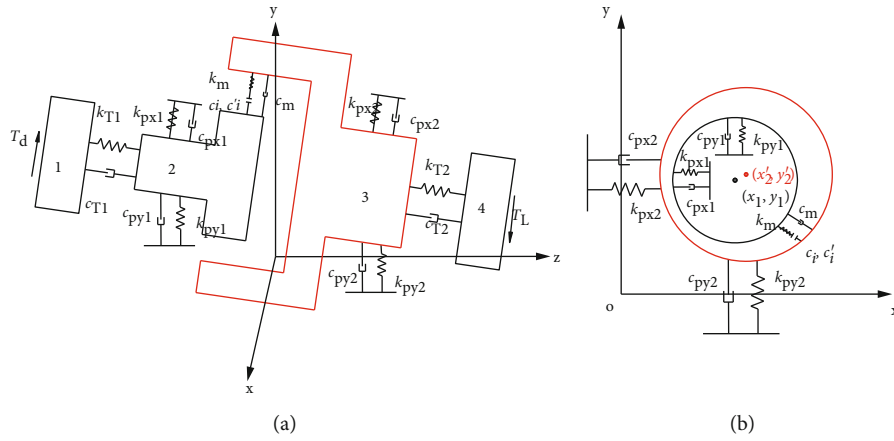
FIGURE 1: The vibration model of the bending–torsion coupling of the involute spline coupling: (a) in the three-dimensional plane; (b) in the xoy plane.
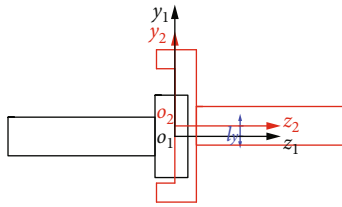
FIGURE 2: Diagram of the parallel misalignment.
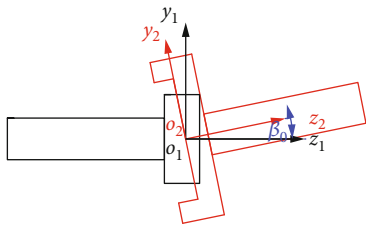
FIGURE 3: Diagram of the angular misalignment.
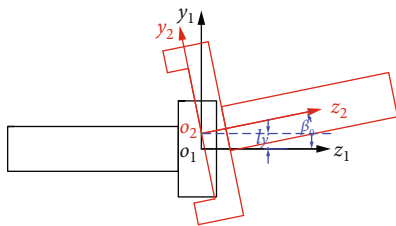
FIGURE 4: Diagram of the combined misalignment.

Figure 3, it can be inferred that the parallel misalignment is formed by moving a distance l along a certain coordinate axis from the initial location. Therefore, in the xoy plane, the coordinate of the y and x direction misalignment of the original internal spline can be expressed as follows:

$$y'_2 = y_2 + l_y, \tag{1}$$

$$x'_2 = x_2 + l_x. \tag{2}$$

2.3. Establishment of Vibration Equations. According to Newton's second law, the vibration equations of the spline coupling in aeroengine are shown in the following equation.

$$
\begin{cases}
J_M \ddot{\theta}_M + k_{T1}(\theta_M - \theta_1) + c_{T1}\left(\dot{\theta}_M - \dot{\theta}_1\right) = T_d \\[4pt]
m_1 \ddot{x}_1 + k_{p1} x_1 + c_{p1} \dot{x}_1 = F_{mx} \\[4pt]
m_1 \ddot{y}_1 + k_{p1} y_1 + c_{p1} \dot{y}_1 = F_{my} - m_1 g \\[4pt]
J_1 \ddot{\theta}_1 + k_{T1}(\theta_1 - \theta_M) + c_{T1}\left(\dot{\theta}_1 - \dot{\theta}_M\right) = T_m \\[4pt]
m_2 \ddot{x}'_2 + k_{p2} x'_2 + c_{p2} \dot{x}'_2 = -F_{mx} \\[4pt]
m_2 \ddot{y}'_2 + k_{p2} y'_2 + c_{p2} \dot{y}'_2 = -F_{my} - m_2 g \\[4pt]
J_2 \ddot{\theta}_2 + k_{T2}(\theta_2 - \theta_L) + c_{T2}\left(\dot{\theta}_2 - \dot{\theta}_L\right) = -T_m \\[4pt]
J_L \ddot{\theta}_L + k_{T2}(\theta_L - \theta_2) + c_{T2}\left(\dot{\theta}_L - \dot{\theta}_2\right) = -T_L,
\end{cases} \tag{3}
$$

where x_1, y_1, and θ_1 are the vibration displacements along the x-axis, y-axis (m), and the torsional displacement around the axis of the external spline (rad), respectively; x_2, y_2, and θ_2 are the vibration displacements along the x-axis, y-axis (m), and the torsional displacement around the axis of the internal spline, respectively (rad); θ_M and θ_L are the torsional displacements of the prime mover and loads (rad), respectively; θ_M and θ_1, θ_1 and θ_2, and θ_2 and θ_L are all not the same due to the torsional deformation of the shaft and the spine teeth. Then, it is assumed that the supporting stiffness and the supporting damping of the external spline and the internal spline are the same in the x and y directions, respectively. It means

$$
\begin{aligned}
k_{\mathrm{px1}} &= k_{\mathrm{py1}} = k_{\mathrm{p1}}, \\
k_{\mathrm{px2}} &= k_{\mathrm{py2}} = k_{\mathrm{p2}}, \\
c_{\mathrm{px1}} &= c_{\mathrm{py1}} = c_{\mathrm{p1}}, \\
c_{\mathrm{px2}} &= c_{\mathrm{py2}} = c_{\mathrm{p2}}.
\end{aligned} \tag{4}
$$

Then, the rigid displacement of Equation (5) requires to be eliminated. Thereafter, Equation (5) is expressed as follows:

$$
\begin{cases}
\ddot{x}_1 + \dfrac{k_{\mathrm{p1}}}{m_1}x_1 + \dfrac{c_{\mathrm{p1}}}{m_1}\dot{x}_1 = \dfrac{F_{\mathrm{mx}}}{m_1} \\[2mm]
\ddot{y}_1 + \dfrac{k_{\mathrm{p1}}}{m_1}y_1 + \dfrac{c_{\mathrm{p1}}}{m_1}\dot{y}_1 = \dfrac{F_{\mathrm{my}}}{m_1} - g \\[2mm]
\ddot{x}'_2 + \dfrac{k_{\mathrm{p1}}}{m_2}x_2 + \dfrac{c_{\mathrm{p1}}}{m_2}\dot{x}'_2 = -\dfrac{F_{\mathrm{mx}}}{m_2} \\[2mm]
\ddot{y}'_2 + \dfrac{k_{\mathrm{p1}}}{m_2}y'_2 + \dfrac{c_{\mathrm{p1}}}{m_2}\dot{y}'_2 = -\dfrac{F_{\mathrm{my}}}{m_2} - g \\[2mm]
\ddot{\Delta}_1 + k_{\mathrm{T1}}\left(\dfrac{1}{J_1}+\dfrac{1}{J_{\mathrm{M}}}\right)\Delta_1 + c_{\mathrm{T1}}\left(\dfrac{1}{J_1}+\dfrac{1}{J_{\mathrm{M}}}\right)\dot{\Delta}_1 = -\dfrac{r_{\mathrm{b}}T_{\mathrm{d}}}{J_{\mathrm{M}}}+\dfrac{r_{\mathrm{b}}}{J_1}T_{\mathrm{m}} \\[2mm]
\ddot{\Delta}_2 + \dfrac{k_{\mathrm{T2}}}{J_2}\Delta_3 - \dfrac{k_{\mathrm{T1}}}{J_1}\Delta_1 + \dfrac{c_{\mathrm{T2}}}{J_2}\dot{\Delta}_3 - \dfrac{c_{\mathrm{T1}}}{J_1}\dot{\Delta}_1 = -r_{\mathrm{b}}T_{\mathrm{m}}\left(\dfrac{1}{J_1}+\dfrac{1}{J_2}\right) \\[2mm]
\ddot{\Delta}_3 + k_{\mathrm{T2}}()\left(\dfrac{1}{J_2}+\dfrac{1}{J_{\mathrm{L}}}\right)\Delta_3 + c_{\mathrm{T2}}\left(\dfrac{1}{J_2}+\dfrac{1}{J_{\mathrm{L}}}\right)\dot{\Delta}_3 = -\dfrac{r_{\mathrm{b}}T_{\mathrm{m}}}{J_2}-\dfrac{r_{\mathrm{b}}T_{\mathrm{L}}}{J_{\mathrm{L}}}.
\end{cases} \tag{5}
$$

In Equation (5), r_{b} is the radius of the base circle of internal and external splines (rad). The angular velocity $\dot{\theta}_{\mathrm{M}}$ of the prime mover is considered to be a constant value, and

$$
\begin{cases}
\Delta_1 = r_b(\theta_1 - \theta_{\mathrm{M}}) \\
\Delta_2 = r_b(\theta_2 - \theta_1) \\
\Delta_3 = r_b(\theta_2 - \theta_L).
\end{cases} \tag{6}
$$

Then, after introducing the dimensionless reference parameters ω, l, Equation (5) becomes dimensionless:

$$
\begin{cases}
\ddot{\bar{x}}_1 + \overline{k_{\mathrm{p1}}}\bar{x}_1 + \overline{c_{\mathrm{p1}}}\dot{\bar{x}}_1 = \overline{F_{\mathrm{mx1}}} \\[1mm]
\ddot{\bar{y}}_1 + \overline{k_{\mathrm{p1}}}\bar{y}_1 + \overline{c_{\mathrm{p1}}}\dot{\bar{y}}_1 = \overline{F_{\mathrm{my1}}} - \bar{g} \\[1mm]
\ddot{\bar{x}}'_2 + \overline{k_{\mathrm{p2}}}\bar{x}'_2 + \overline{c_{\mathrm{p2}}}\dot{\bar{x}}'_2 = \overline{F_{\mathrm{mx2}}} \\[1mm]
\ddot{\bar{y}}'_2 + \overline{k_{\mathrm{p2}}}\bar{y}'_2 + \overline{c_{\mathrm{p2}}}\dot{\bar{y}}'_2 = \overline{F_{\mathrm{my2}}} - \bar{g} \\[1mm]
\ddot{\bar{\Delta}}_1 + \overline{k_{\mathrm{T1}}}\bar{\Delta}_1 + \overline{c_{\mathrm{T1}}}\dot{\bar{\Delta}}_1 = \bar{T}_1 \\[1mm]
\ddot{\bar{\Delta}}_2 + \overline{k_{\mathrm{T23}}}\bar{\Delta}_3 - \overline{k_{\mathrm{T21}}}\bar{\Delta}_1 + \overline{c_{\mathrm{T23}}}\dot{\bar{\Delta}}_3 - \overline{c_{\mathrm{T21}}}\dot{\bar{\Delta}}_1 = -\bar{T}_2 \\[1mm]
\ddot{\bar{\Delta}}_3 + \overline{k_{\mathrm{T3}}}\bar{\Delta}_3 + \overline{c_{\mathrm{T3}}}\dot{\bar{\Delta}}_3 = -\bar{T}_3.
\end{cases} \tag{7}
$$

In Equation (7),

$$
\begin{aligned}
&\overline{k_{\mathrm{p1}}} = \frac{k_{\mathrm{p1}}}{m_1\omega^2}, \overline{c_{\mathrm{p1}}} = \frac{c_{\mathrm{p1}}}{m_1\omega}, \overline{k_{\mathrm{p2}}} = \frac{k_{\mathrm{p2}}}{m_2\omega^2}, \overline{c_{\mathrm{p2}}} = \frac{c_{\mathrm{p2}}}{m_2\omega} \\[2mm]
&\overline{k_{\mathrm{T1}}} = \frac{k_{\mathrm{T1}}}{\omega^2}\left(\frac{1}{J_1}+\frac{1}{J_{\mathrm{M}}}\right), \overline{k_{\mathrm{T3}}} = \frac{k_{\mathrm{T2}}}{\omega^2}\left(\frac{1}{J_2}+\frac{1}{J_{\mathrm{L}}}\right); \overline{c_{\mathrm{T1}}} = \frac{c_{\mathrm{T1}}}{\omega}\left(\frac{1}{J_1}+\frac{1}{J_{\mathrm{M}}}\right), \overline{c_{\mathrm{T3}}} = \frac{c_{\mathrm{T2}}}{\omega}\left(\frac{1}{J_2}+\frac{1}{J_{\mathrm{L}}}\right) \\[2mm]
&\overline{k_{\mathrm{T21}}} = \frac{k_{\mathrm{T1}}}{J_1\omega^2}, \overline{k_{\mathrm{T23}}} = \frac{k_{\mathrm{T2}}}{J_2\omega^2}; \overline{c_{\mathrm{T21}}} = \frac{c_{\mathrm{T1}}}{J_1\omega}, \overline{c_{\mathrm{T23}}} = \frac{c_{\mathrm{T2}}}{J_2\omega} \\[2mm]
&L = \frac{l}{r_{\mathrm{b}}} \\[2mm]
&\ddot{\bar{x}}_1 = \frac{\dot{x}_1}{l\omega^2}, \dot{\bar{x}}_1 = \frac{\dot{x}_1}{l\omega}, \bar{x}_1 = \frac{x_1}{l}; \ddot{\bar{x}}_2 = \frac{\ddot{x}_2}{l\omega^2}, \dot{\bar{x}}_2 = \frac{\dot{x}_2}{l\omega}, \bar{x}_2 = \frac{x_2}{l}; \\[2mm]
&\ddot{\bar{y}}_1 = \frac{\ddot{y}_1}{l\omega^2}, \dot{\bar{y}}_1 = \frac{\dot{y}_1}{l\omega}, \bar{y}_1 = \frac{y_1}{l}; \ddot{\bar{y}}_2 = \frac{\ddot{y}_2}{l\omega^2}, \dot{\bar{y}}_2 = \frac{\dot{y}_2}{l\omega}, \bar{y}_2 = \frac{y_2}{l} \\[2mm]
&\ddot{\bar{\Delta}}_1 = \frac{\ddot{\Delta}_1}{l\omega^2}, \dot{\bar{\Delta}}_1 = \frac{\dot{\Delta}_1}{l\omega}, \bar{\Delta}_1 = \frac{\Delta_1}{l} \\[2mm]
&\overline{F_{\mathrm{mx1}}} = \frac{F_{\mathrm{mx}}}{m_1 l\omega^2}; \overline{F_{\mathrm{my1}}} = \frac{F_{\mathrm{my}}}{m_1 l\omega^2}; \overline{F_{\mathrm{mx2}}} = \frac{F_{\mathrm{mx}}}{m_2 l\omega^2}; \overline{F_{\mathrm{my2}}} = \frac{F_{\mathrm{my}}}{m_2 l\omega^2}; \\[2mm]
&\bar{T}_1 = \frac{r_{\mathrm{b}}T_{\mathrm{m}}}{J_1 l\omega^2} - \frac{r_{\mathrm{b}}T_{\mathrm{d}}}{J_{\mathrm{M}} l\omega^2}; \bar{T}_2 = r_{\mathrm{b}}T_{\mathrm{m}}\left(\frac{1}{J_1 l\omega^2}+\frac{1}{J_2 l\omega^2}\right); \bar{T}_3 = \frac{r_{\mathrm{b}}T_{\mathrm{m}}}{J_2 l\omega^2} - \frac{r_{\mathrm{b}}T_{\mathrm{L}}}{J_{\mathrm{L}} l\omega^2}.
\end{aligned} \tag{8}
$$

3. Analysis of the Nonlinear Vibration Force

The component of the total meshing force along the coordinate axis can be obtained by a discrete summation of the forces along the meshing line of a single pair of teeth. The total meshing torque is the total meshing force multiplied by the radius of the base circle r_b. The calculation is shown in following equation:

$$\begin{cases} F_{mx} = -\sum_{i=1}^{z} F_{ni} \sin \varphi_i \\ F_{my} = \sum_{i=1}^{z} F_{ni} \cos \varphi_i \\ T_m = r_b \sum_{i=1}^{z} F_{ni}, \end{cases} \quad (9)$$

where F_{ni} is the meshing force of a single pair of teeth along the meshing line as shown in the following equation:

$$F_{ni} = k_m g_i[\Delta n_i(t)] + c_m \dot{g}_i[\Delta n_i(t)]. \quad (10)$$

Here, $g_i[\Delta n_i(t)]$ is the meshing deformation function. It is assumed that the initial clearance on both sides of each tooth of internal and external splines is c_i and c'_i, respectively (if the center deviation of the spline shaft is not considered, $c_i = c'_i$), and the meshing deformation function and its differential function (Equations (11) and (12)) are all piecewise functions.

When there is no fretting wear between the spline teeth, the meshing deformation function and its differential function are expressed as follows:

$$g_i[\Delta n_i(t)] = \begin{cases} \Delta n_i(t) - c'_i & \Delta n_i(t) > c'_i \\ 0 & -c_i \leq \Delta n_i(t) \leq c'_i \\ \Delta n_i(t) + c_i & \Delta n_i(t) < -c_i, \end{cases} \quad (11)$$

$$\dot{g}_i[\Delta n_i(t)] = \begin{cases} \dot{\Delta n}_i(t) & \Delta n_i(t) > c'_i \& \Delta n_i(t) < -c_i \\ 0 & -c_i \leq \Delta n_i(t) \leq c'_i. \end{cases} \quad (12)$$

However, the involute spline coupling of aeroengine is accompanied by severe fretting wear during its operation. When the wear depth is considered, the original backlash of the spline coupling changes, that is, if the wear depth of each tooth is h_i, $i = 1, 2, 3 \cdots z$, then the initial backlash of one side on-meshing of the aviation involute spline considering the fretting wear becomes $c_i + h_i$. Hence, the expression of $g_i[\Delta n_i(t)]$ becomes

$$g_i[\Delta n_i(t)] = \begin{cases} \Delta n_i(t) - c'_i & \Delta n_i(t) > c'_i \\ 0 & -(c_i + h_i) \leq \Delta n_i(t) \leq c'_i \\ \Delta n_i(t) + (c_i + h_i) & \Delta n_i(t) < -(c_i + h_i), \end{cases}$$

$$\dot{g}_i[\Delta n_i(t)] = \begin{cases} \dot{\Delta n}_i(t) & \Delta n_i(t) > c'_i \& \Delta n_i(t) < -(c_i + h_i) \\ 0 & -(c_i + h_i) \leq \Delta n_i(t) \leq c'_i. \end{cases}$$
$$(13)$$

If the misalignment of the spline shaft is not considered, $c_i = c'_i$, according to the deformation formula of a single tooth (Equation (11)), the relative displacement on the meshing line $\Delta n_i(t)$ is also required to obtain the vibration meshing force. Thus, the involute profile is simplified as
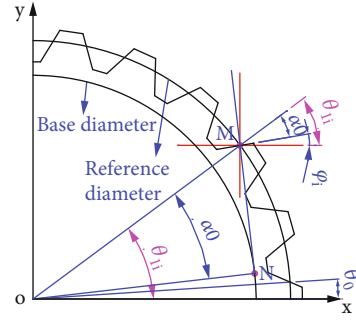
FIGURE 5: Diagram of the related angle.

trapezoid. It is observed that it is negative while moving inward the tooth along the meshing line on the working profile and it is positive while moving outward the tooth along the meshing line on the working profile. All the lengths of the segment involved below are positive as well. Then, α_0 is the pressure angle on the reference circle (rad); z is the total number of teeth; i is the tooth number (set the tooth on the x-axis at the initial time as the first pair of teeth, and the numbers of the rest of the teeth are 1, 2, and 3 in sequence); ω is the angle velocity (rad/s); t is the time (s); θ_0 is the half angle of the tooth thickness of the reference circle (rad), $\theta_0 = \pi/2z$; the angle φ_i between the working profile and the x direction is defined as follows:

$$\varphi_i = \theta_i - \alpha_0. \quad (14)$$

θ_i is the angle of a tooth at a certain time which can be expressed as follows:

$$\theta_i = 2\pi i/z + \omega_0 t + \theta_0 \ (\theta_0 = \pi/2z), \quad (15)$$

as shown in Figure 5.

The formula of the displacement along the meshing line is expressed as follows:

$$\Delta n_1 = -x_1 \sin \varphi_i + y_1 \cos \varphi_i. \quad (16)$$

It can be concluded that the displacement formulas on the meshing line of the external and internal splines are the same for the φ_i of different quadrants and for different modes of movement; when considering the misalignment, they are expressed as follows:

$$\Delta n_1 = -x_1 \sin \varphi_i + y_1 \cos \varphi_i,$$
$$\Delta n_2 = -x'_2 \sin \varphi_i + y'_2 \cos \varphi_i. \quad (17)$$

Based on the above discussion, the formula for the relative displacement on meshing lines between the internal and external splines without considering the misalignment is expressed as follows:
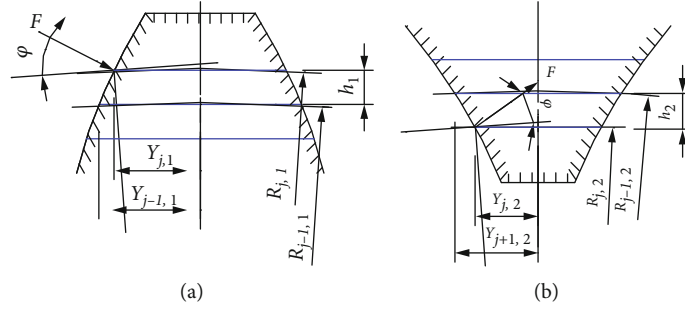
FIGURE 6: Schematic diagram of the loaded involute spline coupling of aeroengine under ideal conditions: (a) schematic diagram of the loaded external spline; (b) schematic diagram of the loaded internal spline.

$$
\begin{aligned}
\Delta n_i(t) &= \Delta n_2(t) - \Delta n_1(t) + r_b(\theta_2 - \theta_1) \\
&= \left(x_1 - x'_2\right)\sin\varphi_i - \left(y_1 - y'_2\right)\cos\varphi_i + r_b(\theta_2 - \theta_1) \\
&= \left(x_1 - x'_2\right)\sin\varphi_i - \left(y_1 - y'_2\right)\cos\varphi_i + \Delta_2.
\end{aligned}
\tag{18}
$$

In this work, the influence of the nonlinear vibration characteristics under the misalignment of the involute spline coupling system is studied. Therefore, the relative displacement $\Delta n_i(t)$ on the meshing line between the involute spline couplings is calculated considering the misalignment. Then, the corresponding equations are expressed by Equations (19) and (20), respectively, as follows:

$$
\Delta n_i(t) = \left(x_1 - x'_2\right)\sin\varphi_i - \left(y_1 - y'_2\right)\cos\varphi_i + \Delta_2, \tag{19}
$$

$$
\begin{aligned}
\dot{\Delta}n_i(t) &= \left(\dot{x}_1 - \dot{x}'_2\right)\sin\left(\frac{2\pi}{z}i + \omega_0 t + \theta_0 - \alpha_0\right) \\
&+ \left(x_1 - x'_2\right)\omega_0\cos\left(\frac{2\pi}{z}i + \omega_0 t + \theta_0 - \alpha_0\right) \\
&- \left(\dot{y}_1 - \dot{y}'_2\right)\cos\left(\frac{2\pi}{z}i + \omega_0 t + \theta_0 - \alpha_0\right) \\
&+ \left(y_1 - y'_2\right)\omega_0\sin\left(\frac{2\pi}{z}i + \omega_0 t + \theta_0 - \alpha_0\right) + \dot{\Delta}_2.
\end{aligned}
\tag{20}
$$

4. Meshing Stiffness of the Spline Coupling

4.1. Meshing Stiffness of the Spline Coupling without Misalignment. It is well known that the loaded position is located at the pitch circle under ideal condition, as shown in Figure 6.

First, the length from the root of the tooth to the location of loading should be evenly divided into an identical microsegment, and then each parameter without considering the transverse vibration is calculated as follows:

The microsegment height is shown in the following:

$$
h'_k = \frac{h_{fk}(h_{a2})}{n}, \tag{21}
$$

where $k = 1, 2$; when it is the external spline, $k = 1$; when it is

the internal spline, $k = 2$. The tooth root height h_{f1} of the external spline and the tooth top height h_{a2} of the internal spline are shown in the following:

$$
\begin{cases}
h_{f1} = 0.5(d_1 - d_{1\ min}) \\
h_{a2} = 0.5(d_{2\ max} - d_2),
\end{cases}
\tag{22}
$$

where d_1 is the diameter of the reference circle of the external spline, $d_{1\ min}$ is the small diameter of the external spline, d_2 is the diameter of the reference circle of the internal spline, and $d_{2\ max}$ is the large diameter of the internal spline.

The thickness of the half tooth of the jth segment for the external and internal splines is expressed by Equation (23) as follows (for the external spline, $Y_{j,k}$ is the thickness of the upper half tooth of the jth segment; for the internal spline, $Y_{j,k}$ is the thickness of the lower half tooth of the jth segment):

$$
Y_{j,k} = 0.5\left(\frac{S\cdot R_{j,k}}{r} \pm 2R_{j,k}\left(\mathrm{inv}(a_0) - \mathrm{inv}\left(a_{j,k}\right)\right)\right), \tag{23}
$$

where S is the tooth thickness of the reference circle, r is the radius of the reference circle, and $\mathrm{inv}(a_0)$ is the involute function of a pressure angle of the reference circle; for a pressure angle of 30°, the formula is shown as follows:

$$
\mathrm{inv}(a_0) = \tan\left(\frac{\pi}{6}\right) - \frac{\pi}{6}. \tag{24}
$$

If $\mathrm{inv}(a_{j,k})$ is the involute function of the pressure angle corresponding to the upper surface of the jth segment, it can be expressed as follows:

$$
\begin{aligned}
\mathrm{inv}\left(a_{j,k}\right) &= \tan\left(a_{j,k}\right) - a_{j,k}, \\
a_{j,k} &= \arccos\left(\frac{r_b}{R_{j,k}}\right),
\end{aligned}
\tag{25}
$$

where r_b is the radius of base circle and $R_{j,k}$ is the upper surface radius of the jth segment.
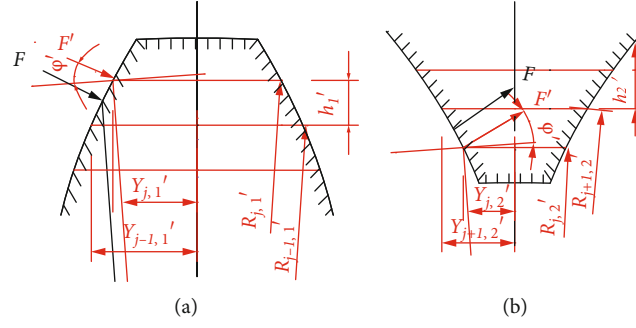
FIGURE 7: Schematic diagram of the loaded spline considering the transverse vibration: (a) schematic diagram of the loaded external spline considering the transverse vibration; (b) schematic diagram of the loaded internal spline considering the transverse vibration.
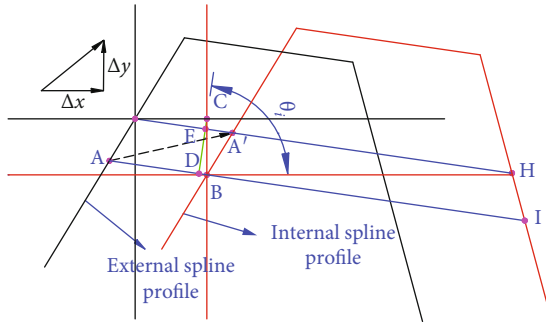
FIGURE 8: Graphic of L_{ed} (considering the external spline as an example, where point A and point A′ are the positions of the engagement points on the external spline before and after the movement).

TABLE 1: vibration parameters of involute spline coupling.

The parameters	The value
Moment of inertia at prime mover, J_M (kg m^2)	7.54×10^{-3}
Load moment of inertia, J_L (kg m^2)	7.5263×10^{-3}
Moment of inertia of external spline, J_1 (kg m^2)	3.4358×10^{-3}
Internal spline moment of inertia, J_2 (kg m^2)	3.7321×10^{-3}
Concentrated mass of external spline, m_1 (kg)	4.5106
Concentrated mass of internal spline, m_2 (kg)	4.5572
Driving torque, T_d (Nm)	30.66
Load moment, T_L (Nm)	28 (light load)
Support stiffness, k_{p1}, k_{p2} (N/m)	5×10^6

The average areas $A_{j,k}$ of the upper and lower surfaces of the jth segment are shown by the following equation:

$$\begin{cases} A_{j,1} = L\left(Y_{j,1} + Y_{j\text{-}1,1}\right) \\ A_{j,2} = L\left(Y_{j,2} + Y_{j+1,2}\right), \end{cases} \tag{26}$$

where L is the tooth width.

For the external spline, the distance from the pitch circle to the upper surface of the jth segment can be expressed as follows:
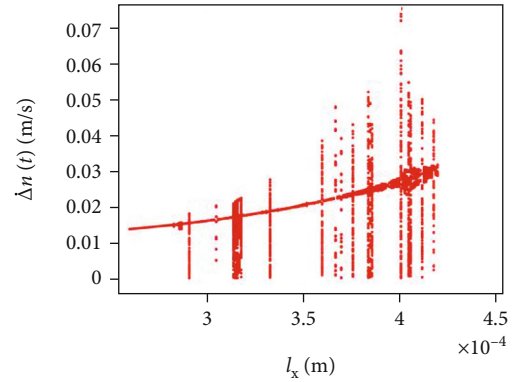
FIGURE 9: Bifurcation diagrams with the misalignment changing of the x direction when the misalignment in the y direction is 1×10^{-5} m.

$$S_{j,1} = r - R_{j,1}. \tag{27}$$

For the internal spline, the distance from the pitch circle to the lower surface of the jth segment is given by

$$S_{j,2} = R_{j,2} - r. \tag{28}$$

The moment of inertia of the jth segment $I_{j,k}$ is given by

$$\begin{cases} I_{j,1} = \dfrac{1}{3}L\left(Y_{j,1}{}^3 + Y_{j\text{-}1,1}{}^3\right) \\ I_{j,2} = \dfrac{1}{3}L\left(Y_{j,2}{}^3 + Y_{j+1,2}{}^3\right). \end{cases} \tag{29}$$

The elastic modulus is given by

$$E_\mu = \frac{E}{1 - \mu^2}. \tag{30}$$

For the involute spline meshing with side, only the tangential stiffness is considered. The deformation of the axial matrix and yield extrusion is ignored. Thus, after the bending and shear flexibility of the single tooth model of the internal and external splines being obtained, the total flexibility is obtained
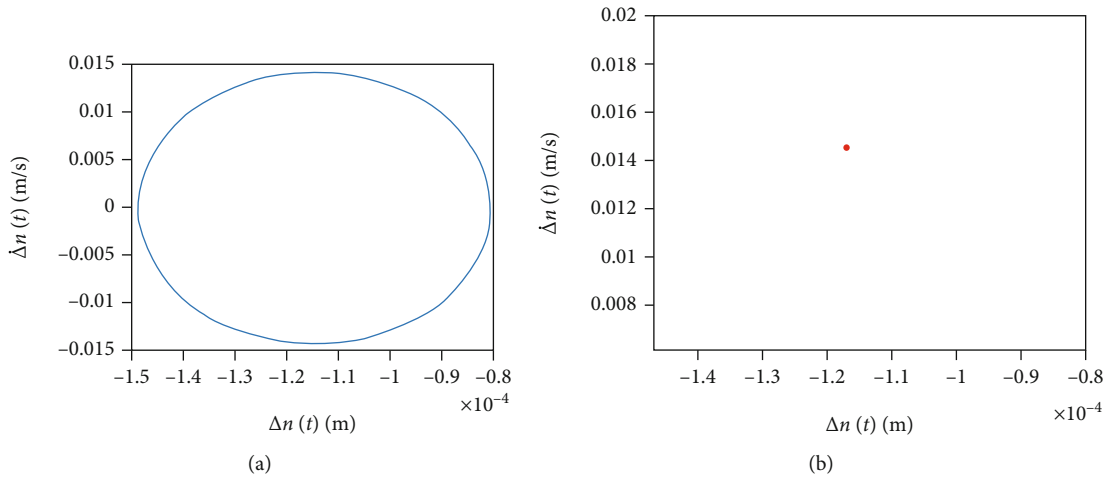
FIGURE 10: When the misalignment in the x direction is 2.73×10^{-4} m: (a) relative displacement velocity and (b) the corresponding diagram of Poincare.
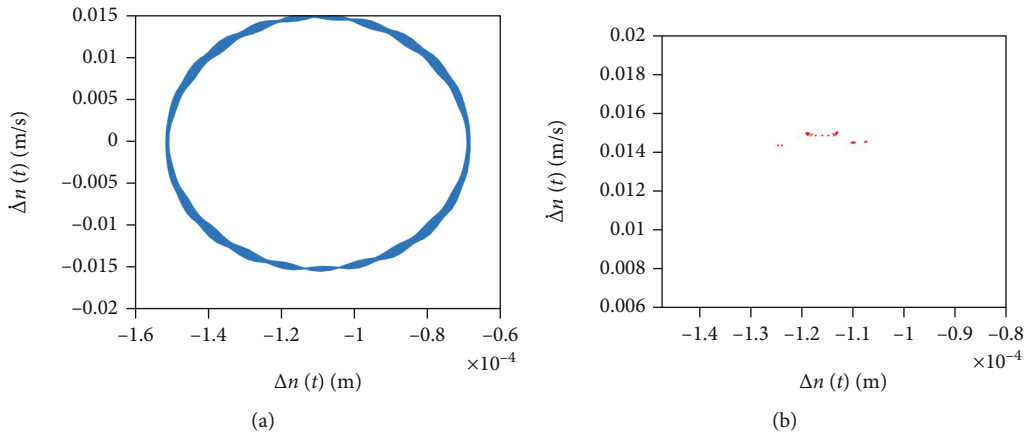
FIGURE 11: When the misalignment in the x direction is 2.83×10^{-4} m: (a) relative displacement velocity and (b) the corresponding diagram of Poincare.
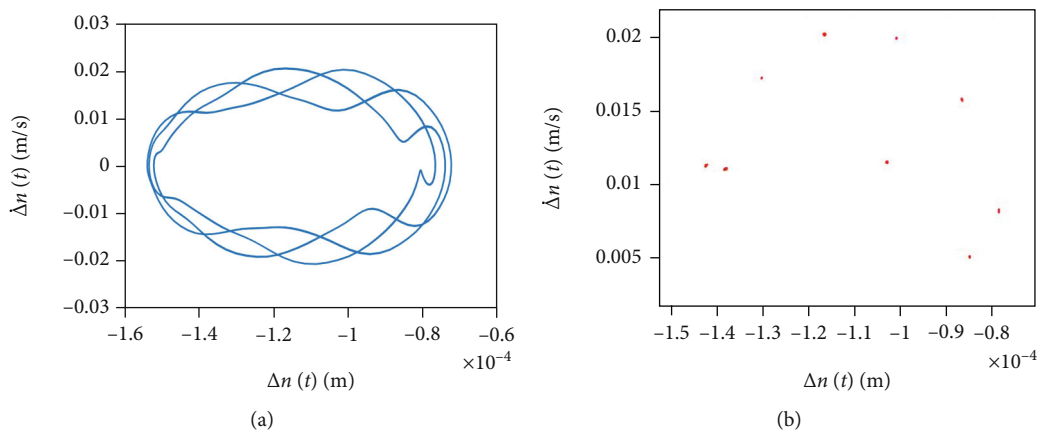
FIGURE 12: When the misalignment in the x direction is 3.05×10^{-4} m: (a) relative displacement velocity and (b) the corresponding diagram of Poincare.
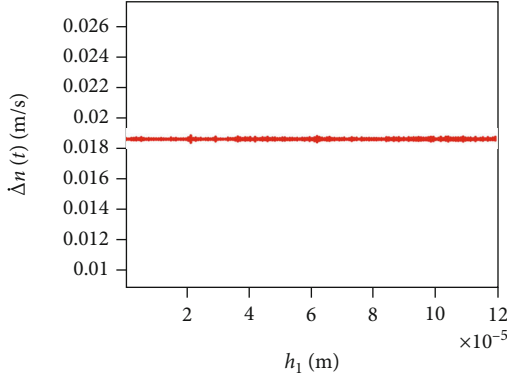
FIGURE 13: Bifurcation diagrams with changes in the uniform wear when the misalignment in the x direction is 3.2×10^{-4} m.
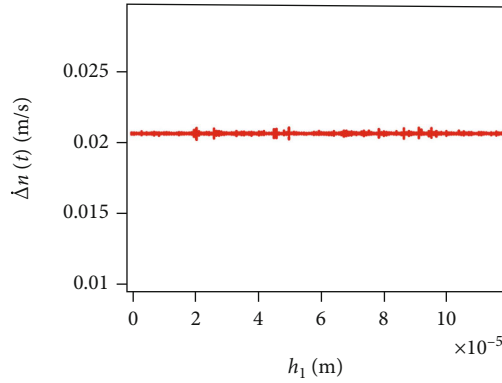
FIGURE 14: Bifurcation diagrams with changes in the uniform wear when the misalignment in the x direction is 3.4×10^{-4} m.

FIGURE 15: Bifurcation diagrams with changes in the uniform wear when the misalignment in the x direction is 3.32×10^{-4} m.
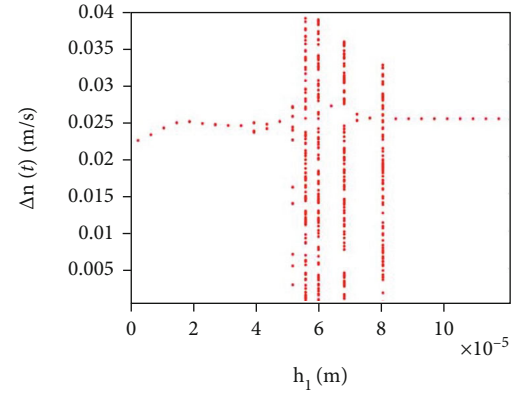
FIGURE 16: Bifurcation diagrams with changes in the wear when the misalignment in the x direction is 2.8×10^{-4} m.

by summing them, and then its derivative is obtained. Finally, the stiffness of the single tooth of the internal and external splines is obtained.

The formula for calculating the bending flexibility is expressed by the following equation:

$$
\Delta_{b,k} = \frac{1}{E_\mu} \left[\frac{\cos^2 \varphi}{3} \sum_{j=1}^{n} \frac{h_k}{I_{j,k}} \left(h_k^2 + 3S_{j,k}h_k + 3S_{j,k}^2 \right) \right.
$$
$$
- Y_F \cos \varphi \sin \varphi \sum_{j=1}^{n} \frac{h_k}{I_{j,k}} \left(h_k + 2S_{j,k} \right) \tag{31}
$$
$$
\left. + Y_F^2 \sin^2 \varphi \sum_{j=1}^{n} \frac{h_k}{I_{j,k}} \right],
$$

where φ is the contact angle of the meshing point, $\phi = \alpha_0$, and Y_F is the thickness of the half tooth of the reference circle, $Y_F = 0.25\pi m$. The formula for calculating the shear flexibility is given by

$$
\Delta_{s,k} = \frac{1.2 \cos^2 \varphi}{G} \sum_{j}^{n} \frac{h_k}{A_{j,k}}. \tag{32}
$$

The total flexibility of a pair of teeth is given by

$$
D_T = D_{b,1} + D_{b,2} + D_{s,1} + D_{s,2}. \tag{33}
$$

The total tangential stiffness of a pair of teeth is given by

$$
K_T = \frac{1}{\Delta_T}. \tag{34}
$$

4.2. Meshing Stiffness of the Spline Coupling with the Misalignment. However, the position of the meshing point (i.e., the position of the loading point) will be changed with the transverse vibration and the parallel misalignment, and thus, the meshing angle, the height of the microtooth, and the half-tooth thickness of the microtooth will also be changed, as well as the stiffness will inevitably change, as shown in Figure 7.

Therefore, the microsegment height changes into the following expression:

$$
h'_k = \frac{h_{fk} + L_{ed}}{n}, \tag{35}
$$

where L_{ed} is the increment of the root (or top) height of the external spline and the internal spline along the microsegment

(a)

(b)
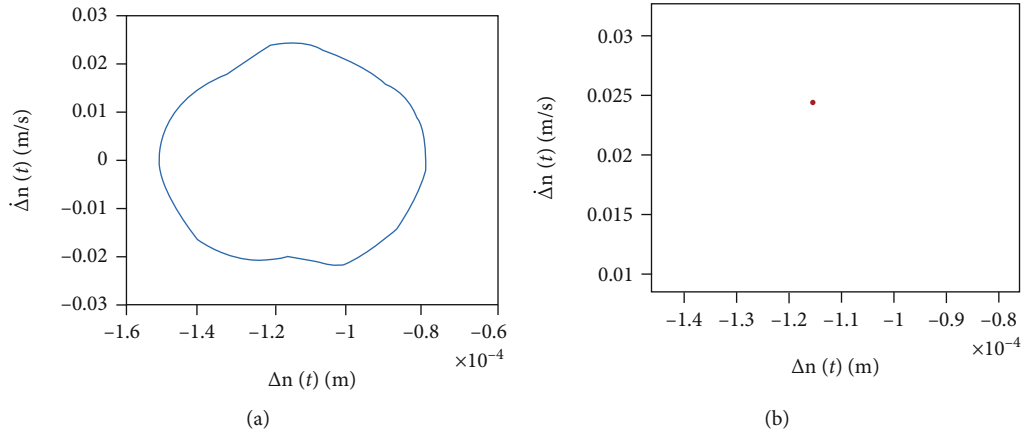
FIGURE 17: When the wear is 1.59×10^{-5} m (the misalignment in the x direction is 2.8×10^{-4} m): (a) relative displacement velocity and (b) the corresponding diagram of Poincare.

(a)

(b)
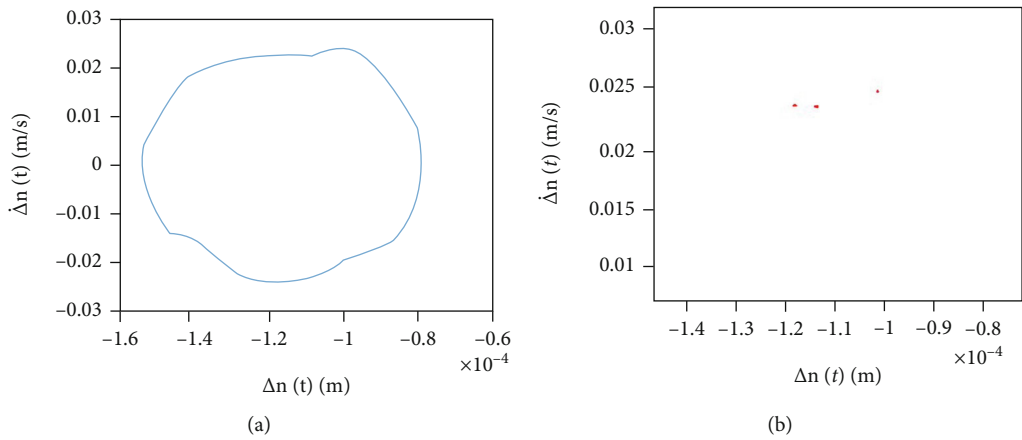
FIGURE 18: When the wear is 3.975×10^{-5} m (the misalignment in the x direction is 2.8×10^{-4} m): (a) relative displacement velocity and (b) the corresponding diagram of Poincare.

(a)

(b)
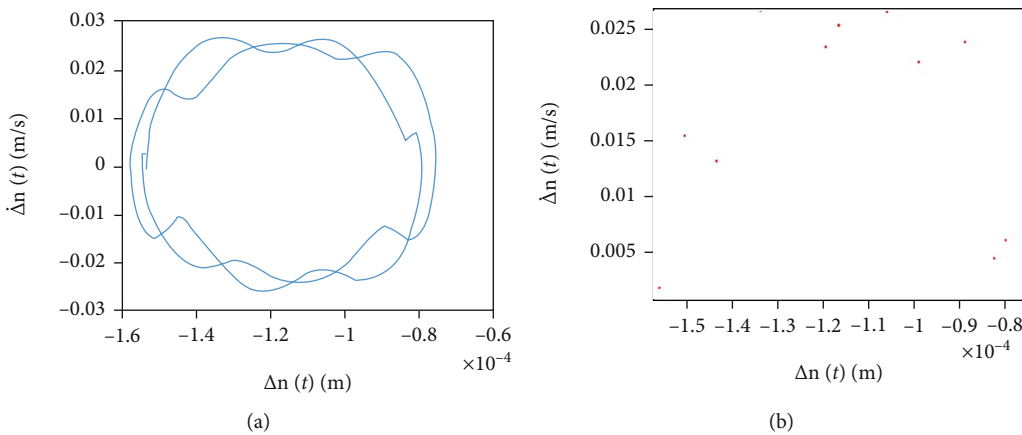
FIGURE 19: When the wear is 5.168×10^{-5} m (the misalignment in the x direction is 2.8×10^{-4} m): (a) relative displacement velocity and (b) the corresponding diagram of Poincare.

(a)

(b)
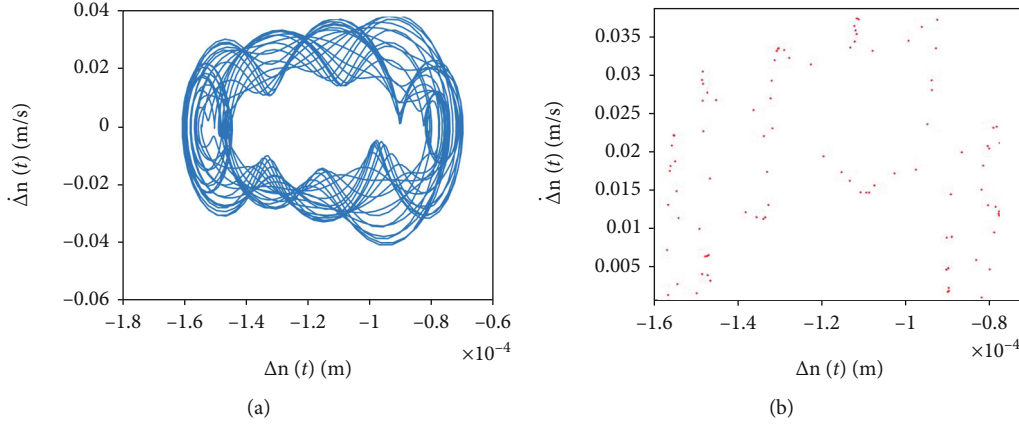
FIGURE 20: When the wear is 5.565×10^{-5} m (the misalignment in the x direction is 2.8×10^{-4} m): (a) relative displacement velocity and (b) the corresponding diagram of Poincare.

direction after the change of the engagement point, which can be expressed as follows:

$$L_{ed} = \Delta x \cos \theta_i + \Delta y \sin \theta_i. \tag{36}$$

It is shown in Figure 8.

When considering the existence of the transverse vibration, for the external spline, the upper and lower surface radii of the jth segment can be expressed as follows:

$$R'_{j,1} = R_{j,1} + L_{ed}, \tag{37}$$

$$R'_{j-1,1} = R_{j-1,1} + L_{ed}. \tag{38}$$

For the internal spline, the upper and lower surface radii of the jth segment are given by

$$R'_{j,2} = R_{j,2} + L_{ed},$$
$$R'_{j+1,2} = R_{j+1,2} + L_{ed}, \tag{39}$$

Accordingly, for external and internal splines, the distance from the pitch circle to the upper and lower surfaces of the jth segment is given by

$$S^{\cdot}_{j,k} = r + L_{ed} - R^{\cdot}_{j,k}. \tag{40}$$

Y_F is given by

$$Y_F{}' = 0.5 \left(\frac{S \cdot (r + L_{ed})}{r} - 2(r + L_{ed}) \left(\text{inv}(a_0) - \text{inv}\left(a_0{}'\right) \right) \right), \tag{41}$$

where $a_0{}'$ is the pressure angle of $(r + Led)$:

$$a_0{}' = \arccos \left(\frac{r_b}{r + L_{ed}} \right). \tag{42}$$

By substituting Equations (35) and (37)–(42) into the corresponding calculation equations, respectively, the single
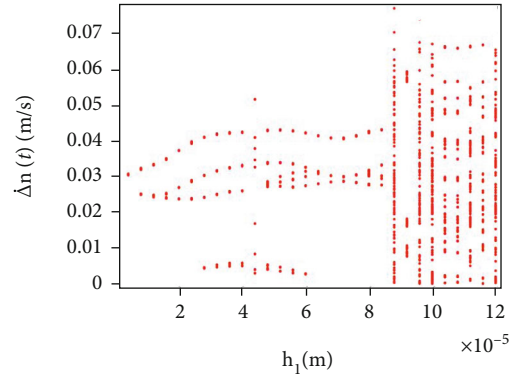
FIGURE 21: Bifurcation diagrams with changes in the wear when the misalignment in the x direction is 3.4×10^{-4} m.

tooth stiffness considering the transverse vibration can be obtained. Finally, the meshing force of the involute spline is obtained too.

The rest of the vibration parameters have been described in an earlier study [5].

5. Nonlinear Vibration Characteristics of the Involute Spline Coupling

In this work, the calculation process of the torsional stiffness k_T and the torsional damping and meshing damping of the spline shaft is adapted from a previous study [31]; and the equivalent diameter of internal and external splines is 30 mm for all; the equivalent length of external and internal splines is 81 and 82 mm, respectively; and the unilateral side clearance of splines is $c_i = c_i' = 7.95 \times 10^{-5}$ m. The rest of the parameters are given in Table 1, the detailed analysis of the nonlinear vibration characteristics of the system under different working conditions is presented in the next sections.

5.1. The Influence of the Misalignment on the Nonlinear Vibration Characteristics of the System. In this work, the relative velocity of a single pair of teeth was analyzed, and it was assumed that there is no wear between the teeth. The

(a)

(b)
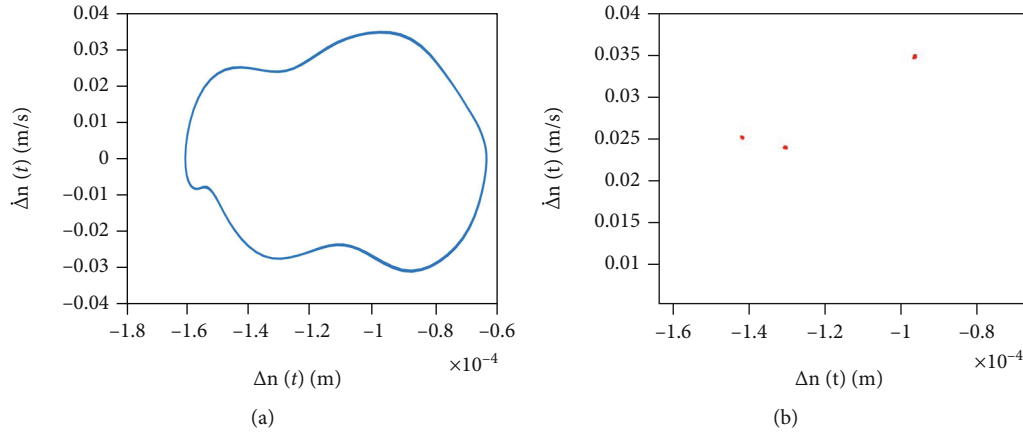
FIGURE 22: When the wear is 1.59×10^{-5} m (the misalignment in the x direction is 3.4×10^{-4} m): (a) relative displacement velocity and (b) the corresponding diagram of Poincare.

rotational speed is 4000 r/min, and the parallel misalignment in the y direction is unchanged with the value of 1×10^{-5} m, and then, the nonlinear vibration characteristics of the system are studied with the misalignment changing in the x direction. Figure 9 shows the bifurcation characteristics of the system as the misalignment changes. From the bifurcation diagram, it can be seen that when the misalignment in the x direction is between 2.6×10^{-4} m and 2.82×10^{-4} m, the system is in a single period, and Figure 10 shows the phase diagram and the Poincare section diagram with these misalignments of x. When the misalignment is 2.83×10^{-4} m, the system is considered to be in a quasiperiodic state, as shown in Figure 11. After a short period of a single period state, when the misalignment is 3.05×10^{-4} m, the system suddenly enters a multiperiod state, as shown in Figure 12, and there are some discrete points in the diagram of the Poincare section. When the misalignment increases to 3.14×10^{-4} m, the system enters a short period of chaos, until the misalignment is 3.19×10^{-4} m, and the system exits the chaos state and enters a single period. When the misalignment is 3.33×10^{-4} m, the system returns back to the chaos state again and then returns to the single cycle motion, until the misalignment increases to 3.6×10^{-4} m, and finally the system enters a long-term chaos, with the corresponding interval range of 3.6×10^{-4} m to 4.18×10^{-4} m. In other words, for the parameters used here, it is not found that the system exits from chaos. The motion state of the system is found to be very unstable in this region. For example, with some misalignment, the system returns to a single period or a quasiperiod state, but in the misalignment of 3.6×10^{-4} m to 3.79×10^{-4} m, the system alternates its state between the single period, multiperiod, and chaos. In the misalignment of 3.79×10^{-4} m to 4.18×10^{-4} m, the system changes its state between the quasiperiod state and the chaos state.

It can be concluded that with an increase in the parallel misalignment, the state of the system becomes more and more complex from the beginning of the single period and then changes its state between the single period, quasiperiod, multiperiod, and chaos state but finally changes its state between the quasiperiod and the chaos state. The number
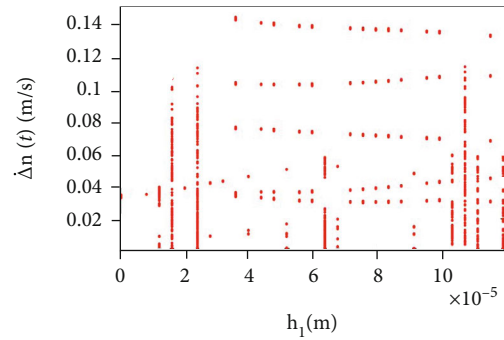
FIGURE 23: Bifurcation diagrams with changes in the wear when the misalignment in the x direction is 3.7×10^{-4} m.

of times the system enters and exits the chaos increases obviously. Therefore, too much misalignment displays a significant impact on the motion state of the system, which makes the system very unstable and then causes damage.

5.2. The Effect of Wear on the Nonlinear Vibration Characteristics of the System with Different Misalignment

5.2.1. The Situation of the Uniform Wear. When the spline is worn, the backlash between the teeth changes, which affects the nonlinear vibration characteristics. Therefore, the nonlinear vibration characteristics with different h_i are analyzed in this work. Here, the rotational speed is 4300 r/min, the misalignment in the y direction is 0.1×10^{-4} m, the support damping in the x and y directions is 2 N s/m for all, and the torsional damping coefficient is 0.005.

At first, it was assumed that the wear amount of each tooth is equal. It means in Equation (12), $h_1 = h_2 = h_3 \cdots = h_i$, and then the influence of the uniform wear on the nonlinear vibration characteristics of the system was analyzed. As shown in Figure 13, when the misalignment in the x direction is 3.2×10^{-4} m, the bifurcation diagram of the system is a straight line under this condition, which indicates that with an increase in the uniform wear of each tooth, the movement state of the system is a single cycle, and there are no obvious
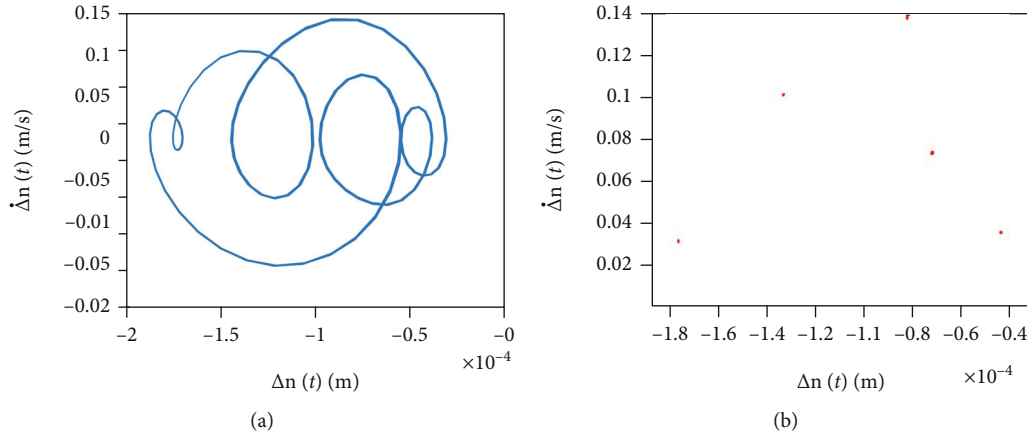
FIGURE 24: When the wear is 4.77×10^{-5} m (the misalignment in the x direction is 3.7×10^{-4} m): (a) relative displacement velocity and (b) the corresponding diagram of Poincare.

changes. When the misalignment in the x direction increases to 3.4×10^{-4} m, the state of the system, as shown in Figure 14, shows no obvious changes as compared to Figure 13. However, as shown in Figure 15, when the misalignment in the x direction approaches some specific values (for example, the misalignment is 3.32×10^{-4} m), the system appears in chaos with an increase in the amount of wear. However, the increase in the wear amount of the teeth in the uniform wear shows no obvious effect on the system state with the working condition given above.

5.2.2. The Situation of the Uneven Wear.

In fact, due to various factors such as the misalignment, mass eccentricity, and manufacturing error, the load on each spline tooth is not the same; in addition to the influence of the vibration, the wear of each spline tooth is not the same consequently. Therefore, it is necessary to analyze the nonlinear vibration characteristics of the involute spline with the nonuniform wear of each tooth. In order to simplify the analysis, it is assumed that the rest of the teeth were not worn; only the first pair of tooth was worn, which took 0.05 times of clearance with an increase in the bifurcation parameter; the wear of the first pair of tooth varied from 0 to 1.5 times of clearance, the rotational speed is 6000 r/min, the misalignment in the y direction is 0.1×10^{-4} m, the support damping in the x and y directions is 5 N s/m for all, and the torsional damping coefficient is 0.007. Then, when the misalignment in the x direction is 2.8×10^{-4} m, the bifurcation diagram of the system with an increase in the amount of wear is shown in Figure 16. It can be seen when the wear is in the range of $0–3.578 \times 10^{-5}$ m (i.e., the wear is in the range of 0–0.45 times of the clearance), the system is in a single period state, as shown in Figure 17; when the wear approaches 3.975×10^{-5} m (i.e., the wear is 0.5 times of the clearance), the system appears in a multiple period bifurcation phenomenon, as shown in Figure 18. From the diagram of Poincare, it can be seen that there are three points on it, and the system is in a three-multiple period state; when the amount of wear is 4.77×10^{-5} m (0.6 times of the clearance), the system returns to the single period state; when the wear increases
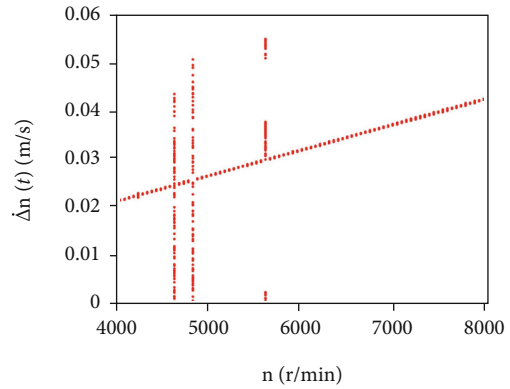
FIGURE 25: Bifurcation diagrams with changes in the rotation speed.

to 5.168×10^{-5} m (0.65 times of the side clearance), as shown in Figure 19, there are several discrete points on the Poincare section, and the system is in a multiperiod state; and when the wear continues to increase to 5.565×10^{-5} m (0.7 times the clearance) as shown in Figure 20, the system begins to enter chaos, and the corresponding Poincare section is scattered. Then, the chaos interval of the system lasts to 7.95×10^{-5} m (1 time of the clearance), which is mixed with a single period and a multiperiod state; when the wear amount increases to 8.348×10^{-5} m (1.05 times of the clearance), the system finally returns to the current periodic state and no longer changes.

Figure 21 shows the bifurcation diagram of the system with an increase in the amount of wear when the misalignment in the x direction increases to 3.434×10^{-4} m. From this figure, it can be seen that when the wear amount is 7.95×10^{-6} m (0.1 times of the clearance), the system appears in a two-period bifurcation; when the wear amount is 1.59×10^{-5} m (0.2 times of the clearance), the system is in a three-period state, as shown in Figure 22. Then, the bifurcation of the system increases gradually, and the state of the system changes from a four-period to a nine-period state. When the wear amount is 8.745×10^{-5} m (1.1 times of the

(a)

(b)
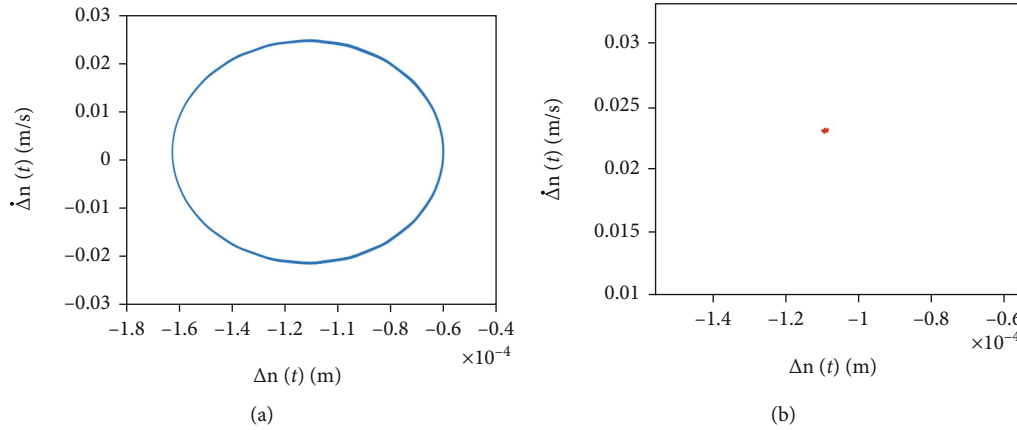
FIGURE 26: When the rotation speed of the system is 4300 r/min: (a) relative displacement velocity and (b) the corresponding diagram of Poincare.

(a)

(b)
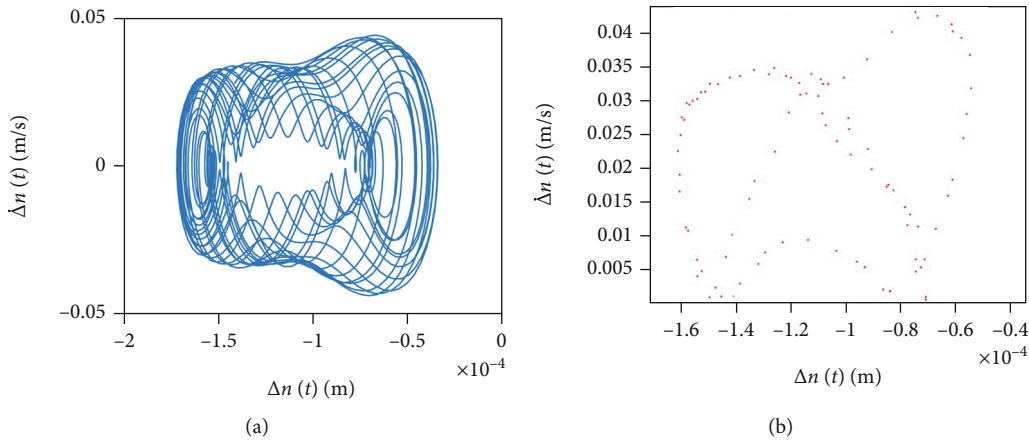
FIGURE 27: When the rotation speed of the system is 4600 r/min: (a) relative displacement velocity and (b) the corresponding diagram of Poincare.

(a)

(b)
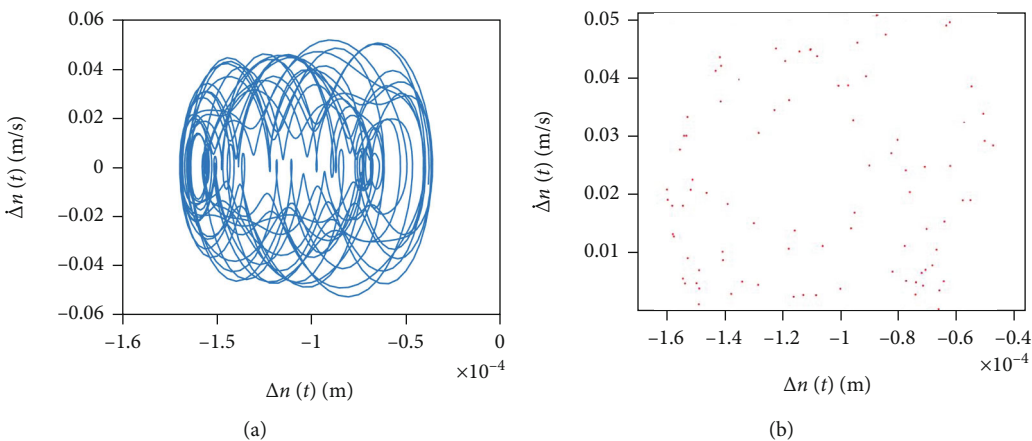
FIGURE 28: When the rotation speed of the system is 4800 r/min: (a) relative displacement velocity and (b) the corresponding diagram of Poincare.

clearance), the system enters chaos. Finally, after the bifurcation point (9.142×10^{-5} m) of the multiperiod state, the system is in the chaos state all the time.

When the misalignment in the x direction increases to 3.7×10^{-4} m, the bifurcation diagram of the system with an

increase in the amount of wear is shown in Figure 23. As compared to Figures 16 and 21, it indicates that the system state of Figure 23 is obviously more complex. It can be seen that with an increase in the amount of wear, the system has experienced the state of the single period, quasi period,

(a)   (b)
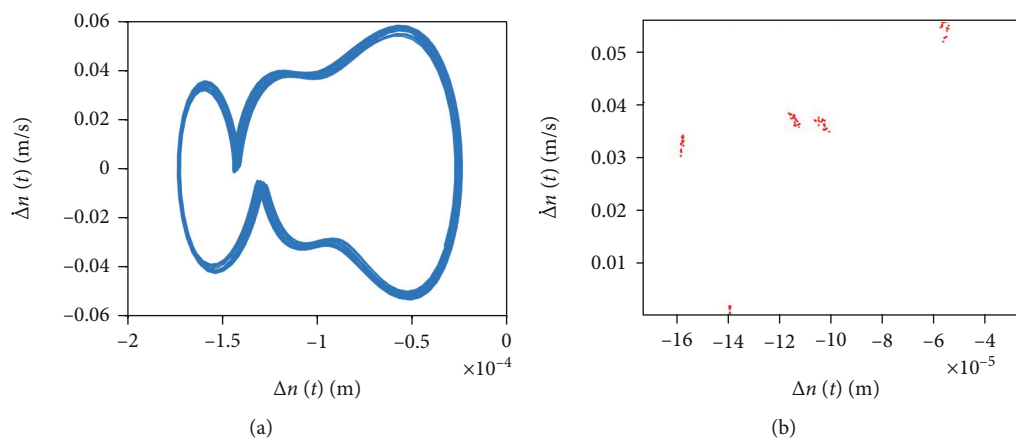
FIGURE 29: When the rotation speed of the system is 5600 r/min: (a) relative displacement velocity and (b) the corresponding diagram of Poincare.
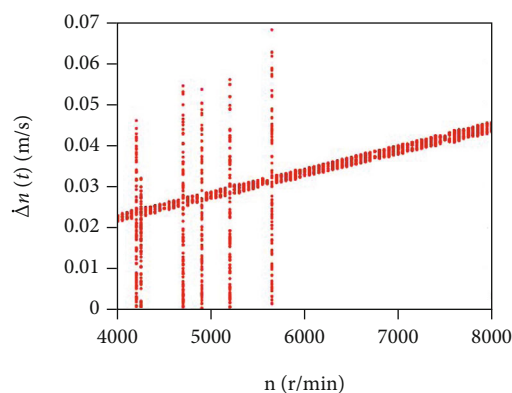
FIGURE 30: Bifurcation diagrams with changes in the rotation speed.

chaos, multiperiod, quasiperiod, and multiperiod and chaos from the initial quasi-periodic state. Within a given range of bifurcation parameters (i.e., the amount of wear), the system finally stays in a chaotic state. It can be concluded that the system behavior is very complex under the condition of large misalignment; the complex movement form causes the fretting effect on the surface of teeth on spline to intensify, which significantly increases the fretting wear failure; and the increase in the amount of wear makes the system movement behavior more complex and thus forms a vicious cycle that is prone to safety accidents. And, when the wear is 4.77×10^{-5} m as shown in Figure 24, the system is getting into quasiperiod.

5.3. The Effect of the Rotational Speed on the Nonlinear Vibration Characteristics of the System with Different Misalignment. When the misalignment in the y direction is 2.4×10^{-4} m and in the x direction is 2.7×10^{-4} m, Figure 25 shows the bifurcation situation of the relative speed of the 22nd teeth on the spline coupling with changes in the rotation speed. In Figure 25, the rotation speed increases from 4000 r/min to 8000 r/min with an increment of 50 r/min. Under this condition of the misalignment, the

state of the system is dominated by a single period motion, but sometimes quasiperiod, double period, and chaos appear at some specific speeds. Figure 26 shows the diagram of the relative displacement velocity on the engagement line and the diagram of Poincare when the rotation speed of the system is 4300 r/min. It can be seen that, in this case, the diagram of the relative displacement velocity is a closed circle, and the corresponding diagram of Poincare is a single point. Obviously, it is a single period motion. With an increase in the rotation speed, the relative velocity on the engagement line shows an upward trend. When the rotation speed of the system is 4600 r/min, from Figure 27, it can be seen that there are a large number of closed curves on the diagram of Poincare and the system is in a quasiperiodic state. When the rotating speed continues to increase, the system returns to the single period state at first, and then the system enters into the chaotic state quickly when the rotating speed is 4800 r/min, as shown in Figure 28. When the rotating speed is 5600 r/min as show in Figure 29, the system enters into the quasiperiodic state again. Moreover, under other rotating speed conditions, the system is in a single period state.

Figure 30 shows the bifurcation situation of the relative speed of the 22nd teeth on the spline coupling with changes in the rotation speed when the misalignment in the y direction is 2.4×10^{-4} m and in the x direction is 2.8×10^{-4} m. From the figure, it can be seen that the system is mainly quasiperiodic (Figure 31 is one of them), and the relative vibration speed between spline pairs increases with an increase in the rotating speed. When the rotating speed is 4200 r/min, 4250 r/min, 4700 r/min, 4900 r/min, 5200 r/min, and 5650 r/min, the system is in a chaotic state for all, as shown in Figure 32 (due to the space limitation, only the diagram when the rotation speed of the system is 4200 r/min is provided in this work).

When the misalignment in the y direction is 2.4×10^{-4} m and in the x direction is 2.9×10^{-4} m, Figure 33 shows the bifurcation situation of the relative speed of the 22nd teeth on the spline coupling with changes in the rotation speed. From the figure, it can be seen that the system is still dominated by a quasiperiodic state, but by comparing with

(a)

(b)
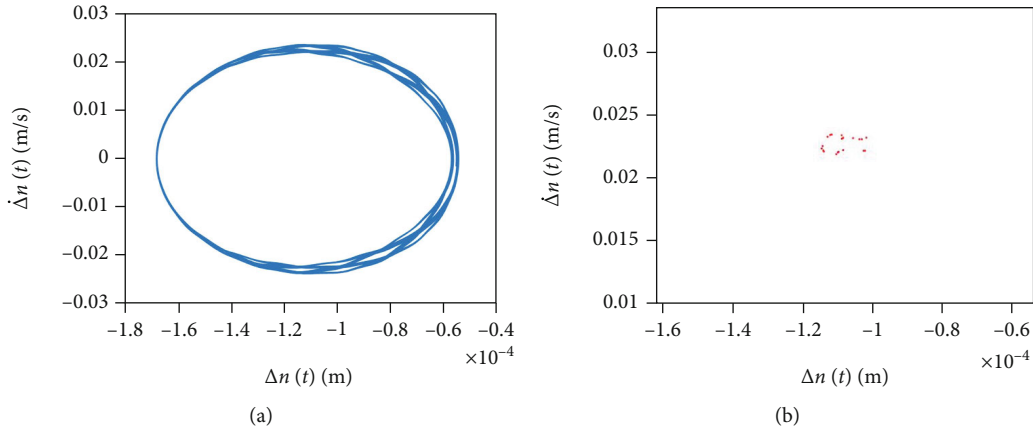
FIGURE 31: When the rotation speed of the system is 4100 r/min: (a) relative displacement velocity and (b) the corresponding diagram of Poincare.

(a)

(b)
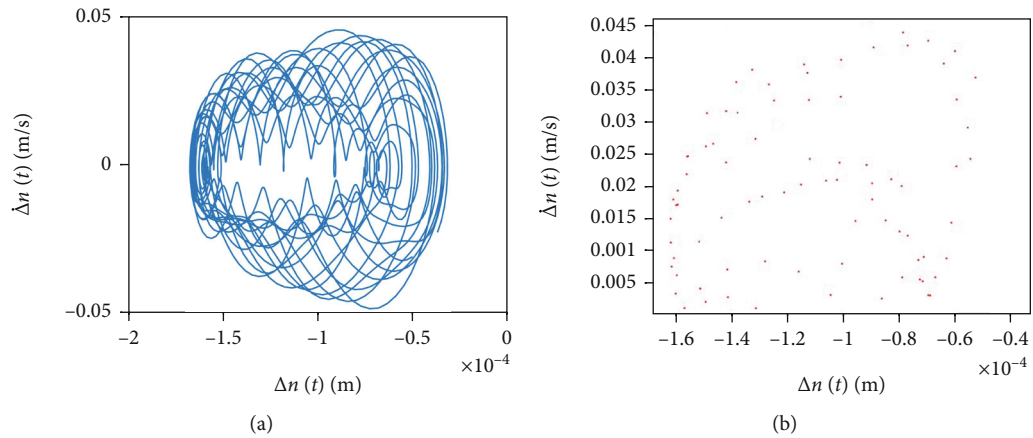
FIGURE 32: When the rotation speed of the system is 4200 r/min: (a) relative displacement velocity and (b) the corresponding diagram of Poincare.
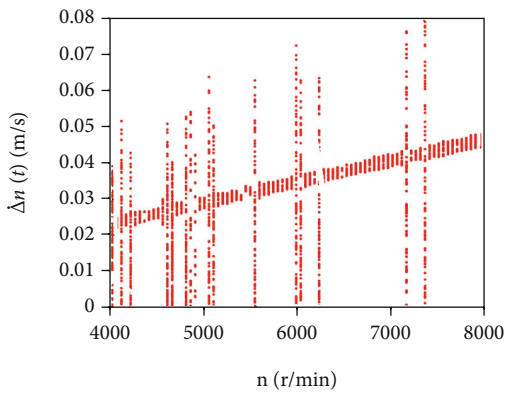
FIGURE 33: Bifurcation diagrams with changes in the rotation speed.

Figure 30, it can be seen that the number of times the system enters into and leaves from the chaotic state has increased obviously. At a specific speed, the system presents a single period state (such as at a speed of 5450 r/min). Therefore, from Figures 25, 30, and 33 it can be concluded that, as the speed continues to increase, the larger the misalignment

is, and the more times the system enters or leaves the chaos state, which easily causes the system to be damaged due to large vibration displacement and speed after suddenly entering the chaos state in the acceleration and deceleration process.

6. Conclusion

In this work, a bending–torsion coupling nonlinear vibration model of the involute spline coupling with the misalignment was proposed, and a dynamic meshing stiffness function with multiteeth engagement was established. Then, the influence of different misalignment and different wear and rotation speeds with different misalignment on the nonlinear vibration characteristics of the involute aviation spline coupling was explored. From the above analysis, the following conclusions are drawn:

(1) For the involute spline coupling without the fretting wear, with an increase in the misalignment, the system gradually becomes unstable, and the number of entering and leaving chaos increases, which easily damages the spline system. However, for the involute spline coupling system with the fretting wear, when

the fretting wear of each tooth is even, it shows a little effect on the behavior of the system

(2) And, when the fretting wear on each tooth increases evenly, the load on each tooth has not changed much, so the excitation generated by the system is not obvious. However, while only one tooth is worn, the increase in the fretting wear of this tooth induces a load difference between this tooth and the rest of the teeth, and then the spline coupling system exhibits lager internal excitation as well as produces complex vibration behavior. This is very detrimental to the stability of the system. Additional, the increase in the misalignment also complicates the vibration of the system under the same fretting wear condition

(3) Furthermore, the increase in the misalignment suddenly increases the number of the state changes as the rotating speed increases. As it is well known, for the mechanical system, the system inevitably experiences increase and decrease in the speed in the process of starting and stopping. When the amount of the misalignment is too large, the system frequently changes its state, so it is easy to induce the large vibration displacement and speed. It demonstrates serious security risks.

Abbreviations

k_{T1}:	Torsional stiffness of external spline
c_{T1}:	Torsional damping of external spline
k_{T2}:	Torsional stiffness of internal spline
c_{T2}:	Torsional damping of internal spline
k_m:	Meshing stiffness
c_m:	Meshing damping
c_i:	Working teeth profiles
c'_i:	Nonworking teeth profiles
k_{p1}:	Supporting stiffness of external spline
k_{p2}:	Supporting stiffness of internal spline
c_{p1}:	Supporting damping of external splines
c_{p2}:	Supporting damping of internal splines
T_d:	Input torque
T_L:	Loading torque
x_1:	Vibrational displacements along the x-axis of external spline
y_1:	Vibrational displacements along the y-axis of external spline
θ_1:	Torsional displacement around the axis of the external spline
x_2:	Vibrational displacements along the x-axis of internal spline
y_2:	Vibrational displacements along the y-axis of internal spline.
θ_2:	Torsional displacement around the axis of the internal spline.
θ_M:	Torsional displacements of the prime motor
θ_L:	Torsional displacements of the load
r_b:	The radius of the base circle of internal and external splines (rad)
$\dot{\theta}_M$:	Constant angular velocity for the prime mover
w:	Nondimensionalizing parameters
l:	Nondimensionalizing parameters
F_{mx}:	Components of the dynamic force along the x
F_{my}:	Components of the dynamic force along the y
m_1:	Mass of external spline
m_2:	Mass of internal spline
J_M:	Moment of inertia of prime mover
J_L:	Moment of inertia of load
J_1:	Moment of inertia of external splin
J_2:	Moment of inertia of internal spline
g:	Gravitational acceleration
Δ:	Deflection
L:	Tooth width
T_d:	Input torque
T_m:	Meshing torque
T_L:	Load torque
F_{ni}:	Meshing force of a single pair of teeth along the meshing line
$g_i[\Delta n_i(t)]$:	Meshing deformation function
$\Delta n_j(t)$:	Equation of relative displacement
h_i:	Wear depth of each tooth
α_0:	Pressure angle of the reference circle
z:	Number of teeth
i:	The tooth number
t:	Time
θ_0:	Half angle of the tooth thickness
θ_i:	Rotation angle of each tooth
φ_i:	Angle between the active tooth profile and the x-axis
ω_0:	Angular velocity
h_{f1}:	The tooth root height
h_{a2}:	The tooth top height
d_1:	The diameter of the reference circle of the external spline
$d_{1\,min}$:	The small diameter of the external spline
d_2:	The diameter of the reference circle of the internal spline
$d_{2\,max}$:	The large diameter of the internal spline.
$Y_{j,k}$:	The thickness of the upper half tooth of the jth segment
S:	The tooth thickness of the reference circle
r:	The radius of the reference circle
$inv(a_0)$:	The involute function of a pressure angle of the reference circle
$R_{j,k}$:	The upper surface radius of the jth segment
$\alpha_{j,k}$:	Pressure angle between the upper surface and tooth profile of the jth segment
$A_{j,k}$:	The average areas
φ:	The contact angle of the meshing point
h_k:	Tooth height of each segment
Y_F:	The thickness of the half tooth of the reference circle
L_{ed}:	The increment of the root (or top) height of the external spline
$I_{j,k}$:	Section moment of inertia of the jth segment
E_μ:	Elastic modulus
E:	Young's modulus.

Data Availability

All data, models, and code generated or used during the study appear in the submitted article.

Conflicts of Interest

The authors declare that there are no conflicts of interest regarding the publication of this paper.

Acknowledgments

References

[1] M. Xu and R. D. Marangoni, "Vibration analysis of a motor-flexible coupling-rotor system subject to misalignment and unbalance, part i: theoretical model and analysis," *Journal of Sound & Vibration*, vol. 176, no. 5, pp. 663–679, 1994.

[2] D. L. Dewell and L. D. Mitchell, "Detection of a misaligned disk coupling using spectrum analysis," *Journal of Vibration and Acoustics*, vol. 106, no. 1, pp. 9–16, 1984.

[3] P. Pennacchi, A. Vania, and S. Chatterton, "Nonlinear effects caused by coupling misalignment in rotors equipped with journal bearings," *Mechanical Systems and Signal Processing*, vol. 30, pp. 306–322, 2012.

[4] K. M. Al-Hussain and I. Redmond, "Dynamic response of two rotors connected by rigid mechanical coupling with parallel misalignment," *Journal of Sound and Vibration*, vol. 249, no. 3, pp. 483–498, 2002.

[5] X. Z. Xue and S. M. Wang, "Dynamic characteristics and load coefficient analysis of involute spline couplings," *Advanced Materials Research*, vol. 889-890, pp. 450–454, 2014.

[6] Y. Wang, G. Zhao, X. Sun, L. I. Shengxiang, and University, D. M., "Review on research of aviation spline," *Aeronautical Manufacturing Technology*, vol. 60, no. 3, pp. 91–100, 2017.

[7] F. Karpat, S. Ekwaro-Osire, K. Cavdar, and F. C. Babalik, "Dynamic analysis of involute spur gears with asymmetric teeth," *International Journal of Mechanical Sciences*, vol. 50, no. 12, pp. 1598–1610, 2008.

[8] F. Karpat and S. Ekwaro-Osire, "Influence of tip relief modification on the wear of spur gears with asymmetric teeth," *Tribology Transactions*, vol. 51, no. 5, pp. 581–588, 2008.

[9] F. Zheng, J. Zhang, L. Yao, and R. Tan, "Investigation on the wear of spur gears generated by modified cutter," *Friction*, vol. 9, no. 2, pp. 288–300, 2021.

[10] G. Li, Z. Wang, and W. Zhu, "Prediction of Surface Wear of Involute Gears Based on a Modified Fractal Method," *Journal of Tribology*, vol. 141, no. 3, 2019.

[11] F. Ke, W. A. Smith, and X. P. Zhong, "Vibration-based updating of wear prediction for spur gears," *Engineering Failure Analysis*, vol. 120, article 105066, 2019.

[12] K. Feng, P. Borghesani, W. A. Smith et al., "Vibration-based updating of wear prediction for spur gears," *Wear*, vol. 426-427, pp. 1410–1415, 2019.

[13] G. Zhao, L. I. Shengxiang, M. Guo, H. Sun, X. Sun, and Q. Han, "Prediction and experiment of vibration wear of aviation spline," *Journal of Aerospace Power*, vol. 12, no. 16, 2018.

[14] C. H. H. Ratsimba, I. R. McColl, E. J. Williams, S. B. Leen, and H. P. Soh, "Measurement, analysis and prediction of fretting wear damage in a representative aeroengine spline coupling," *Wear*, vol. 257, no. 11, pp. 1193–1206, 2004.

[15] J. J. Madge, S. B. Leen, and P. H. Shipway, "The critical role of fretting wear in the analysis of fretting fatigue," *Wear*, vol. 263, no. 1-6, pp. 542–551, 2007.

[16] J. Ding, I. R. McColl, and S. B. Leen, "The application of fretting wear modelling to a spline coupling," *Wear*, vol. 262, no. 9-10, pp. 1205–1216, 2007.

[17] C. Nataraj and K. Kappaganthu, "Nonlinear response in a rotor system with a coulomb spline," *Springer*, vol. 16, pp. 105–120, 2010.

[18] H. L. Li, Y. S. Chen, L. Hou, and Z. Y. Zhang, "Periodic response analysis of a misaligned rotor system by harmonic balance method with alternating frequency/time domain technique," *Science China Technological Sciences*, vol. 59, no. 11, pp. 1717–1729, 2016.

[19] M. Li and L. Yu, "Analysis of the coupled lateral torsional vibration of a rotor-bearing system with a misaligned gear coupling," *Journal of Sound and Vibration*, vol. 243, no. 2, pp. 283–300, 2001.

[20] G. L. Yang, L. L. Zhu, L. C. Zhao, and W. Wang, "Axial system angle misalignment analysis of radial vibration characteristics," *Machinery Design & Manufacture*, vol. A01, pp. 125-126, 2018.

[21] F. W. D. S. Tuckmantel and K. L. Cavalca, "Vibration signatures of a rotor-coupling-bearing system under angular misalignment," *Mechanism & Machine Theory*, vol. 133, pp. 559–583, 2019.

[22] X. Su, H. Lu, X. Zhang, W. Fan, and Y. Zhang, "Analysis of dynamic characteristic for misalignment-spline gear shaft based on whole transfer matrix method," *Journal of Vibroengineering*, vol. 20, no. 3, pp. 1392–1408, 2018.

[23] V. Cuffaro, F. Curà, and A. Mura, "Test rig for spline couplings working in misaligned conditions," *Journal of Tribology*, vol. 136, no. 1, article 011104, 2014.

[24] A. Kahraman, "A spline joint formulation for drive train torsional dynamic models," *Journal of Sound and Vibration*, vol. 241, no. 2, pp. 328–336, 2001.

[25] S. B. Leen, I. J. Richardson, I. R. Mccoll, E. J. Williams, and T. R. Hyde, "Macroscopic fretting variables in a splined coupling under combined torque and axial load," *Journal of Strain Analysis for Engineering Design*, vol. 36, no. 5, pp. 481–497, 2001.

[26] S. Medina and A. V. Olver, "Regimes of contact in spline couplings," *Journal of Tribology*, vol. 124, no. 2, pp. 351–357, 2002.

[27] I. R. Mccoll, J. Ding, and S. B. Leen, "Finite element simulation and experimental validation of fretting wear," *Wear*, vol. 256, no. 11-12, pp. 1114–1127, 2004.

[28] J. Ding, S. B. Leen, and I. R. Mccoll, "The effect of slip regime on fretting wear-induced stress evolution," *International Journal of Fatigue*, vol. 26, no. 5, pp. 521–531, 2004.

[29] G. Zhao, Z. S. Liu, F. Chen, and Y. L. Wang, "Influences of spline coupling on stability of rotor-bearing system," *Zhendong Gongcheng Xuebao/Journal of Vibration Engineering*, vol. 22, no. 3, pp. 280–286, 2009.

[30] G. Zhao, Z. Liu, and F. Chen, "Meshing force of misaligned spline coupling and the influence on rotor system," *International Journal of Rotating Machinery*, vol. 2008, Article ID 321308, 28 pages, 2008.

[31] X. Xue, S. Wang, J. He, and H. Wu, *Investigation of Load Distribution among Teeth of an Aero-engine Spline Coupling*, Springer, 2016.